JGR Solid Earth

RESEARCH ARTICLE
10.1029/2023JB028313

Source Parameters of Laboratory Acoustic Emission Events Estimated From the Coda of Waveforms

Tatiana I. Kartseva[1,2], Nikolai M. Shapiro[1], Andrey V. Patonin[3], Natalia M. Shikhova[3], Vladimir B. Smirnov[2,4], and Alexander V. Ponomarev[2]

[1]Institut des Sciences de la Terre, University Grenoble Alpes, CNRS, University Savoie Mont Blanc, IRD, University Gustave Eiffel, Grenoble, France, [2]Schmidt Institute of Physics of the Earth, Russian Academy of Sciences, Moscow, Russia, [3]CPGR Geophysical Observatory "Borok", Borok, Russia, [4]Faculty of Physics, Lomonosov Moscow State University, Moscow, Russia

Key Points:

- Coda of acoustic emission (AE) waveforms can be used for the source characterization
- Scaling between the corner frequency f_c and seismic moment M_0 varies in function of loading regime and rock type
- The $M_0 - f_c$ scaling of AE events was found similar to that of tectonic earthquakes when isotropic confining pressure applied to intact rocks

Correspondence to:

T. I. Kartseva,
tatiana.kartseva@univ-grenoble-alpes.fr

Citation:

Kartseva, T. I., Shapiro, N. M., Patonin, A. V., Shikhova, N. M., Smirnov, V. B., & Ponomarev, A. V. (2024). Source parameters of laboratory acoustic emission events estimated from the coda of waveforms. *Journal of Geophysical Research: Solid Earth*, *129*, e2023JB028313. https://doi.org/10.1029/2023JB028313

Received 17 NOV 2023
Accepted 20 MAR 2024

Author Contributions:

Conceptualization: Tatiana I. Kartseva, Nikolai M. Shapiro, Vladimir B. Smirnov
Data curation: Tatiana I. Kartseva, Andrey V. Patonin, Natalia M. Shikhova
Formal analysis: Tatiana I. Kartseva, Andrey V. Patonin, Natalia M. Shikhova
Funding acquisition: Nikolai M. Shapiro, Vladimir B. Smirnov, Alexander V. Ponomarev
Investigation: Tatiana I. Kartseva, Andrey V. Patonin, Natalia M. Shikhova
Methodology: Tatiana I. Kartseva, Nikolai M. Shapiro
Project administration: Nikolai M. Shapiro, Vladimir B. Smirnov, Alexander V. Ponomarev
Resources: Nikolai M. Shapiro, Vladimir B. Smirnov, Alexander V. Ponomarev

Abstract We develop a method to estimate relative seismic moments M_0 and corner frequencies f_c of acoustic emission events recorded in laboratory experiments from amplitude spectra of signal's coda composed of reverberated and scattered waves. This approach has several advantages with respect to estimations from direct waves that are often clipped and also are difficult to separate in experiments performed on small samples. Also, inversion of the coda spectra does not require information about the source locations and mechanisms. We use the developed method to analyze the data of two experiments: (a) on granite from the Voronezh crystal massif and (b) on Berea sandstone. The range of absolute corner frequencies estimated in both experiments is around 70 − −700 kHz. The range of relative seismic moments covers $10^{3.5}$. The relation between f_c and M_0 observed on the first stages of both experiments, consisted of increasing isotropic confining pressure, approximately follow $M_0 \sim f_c^{-3}$ scaling and the *b-value* of the Gutenberg-Richter distribution was found close to 1. This can be interpreted as rupturing of preexisting material defects with a nearly constant stress-drop and has a similarity with observations of "natural" earthquakes. Deviations from this "earthquake-like" behavior observed after applying axial loading and initiation of sample damaging can be interpreted as changes in stress-drop. Lower stress-drops prevail for sandstone and higher for granite sample respectively that can be related to the strength of corresponding material.

Plain Language Summary Earthquakes generation mechanisms and conditions favoring their occurrence are still debated. Inability to observe these processes in–situ and long lasting earthquake preparation period favor using laboratory experiments to verify quickly the adequacy of proposed hypotheses. Fracturing of small rock samples with high pressures and recording acoustic waves from their micro-fractures is among them. In most cases, the laboratory acoustic emission (AE) is analyzed and compared to natural seismicity statistically, demonstrating similar Gutenberg-Richter power-law magnitude distribution. More advanced analyses can include source characteristics (corner frequencies, seismic moments, and stress-drops), responsible for the source size, forces acting there and stress changes. Ensembles of these characteristics can give ideas on the common generation mechanisms. In laboratory, several technical limitations slow down the implementation of such analyses, widely used in Earth's seismology. We propose a method that use coda waves (signal's decaying part) to estimate source parameters of the laboratory AE. We tested it on two similar experiments conducted on different rock types. Source analyses revealed the high similarity of well-studied tectonic earthquakes and fracturing of pre-existing inhomogeneties in the rock samples by applying equally distributed external pressure to it. The active production of new fractures under high one-directional pressure in contrary deviated significantly.

1. Introduction

Since early studies in 1960s (e.g., Scholz, 1968), impulsive acoustic emission events observed during the rock physics experiments are often considered as analog of natural earthquakes and are used to study the seismogenic processes in controlled laboratory conditions (e.g., Bolton et al., 2023; Lockner et al., 1991; Marty et al., 2023; McLaskey & Kilgore, 2013; V. B. Smirnov et al., 2019; Yoshimitsu et al., 2014). Analyses of large catalogs of "laboratory earthquakes" demonstrated that they obey statistical distributions similar to "natural" earthquakes. The size-frequency distribution of acoustic emission events follows the power-law Gutenberg Richter relationship (Gutenberg & Richter, 1944) and exhibit aftershock sequences governed by the Omori law (Omori, 1894).

Software: Tatiana I. Kartseva, Nikolai M. Shapiro, Andrey V. Patonin, Natalia M. Shikhova, Vladimir B. Smirnov
Supervision: Nikolai M. Shapiro
Validation: Tatiana I. Kartseva, Nikolai M. Shapiro, Andrey V. Patonin, Natalia M. Shikhova, Vladimir B. Smirnov, Alexander V. Ponomarev
Visualization: Tatiana I. Kartseva, Nikolai M. Shapiro
Writing – original draft: Tatiana I. Kartseva
Writing – review & editing: Nikolai M. Shapiro, Andrey V. Patonin, Natalia M. Shikhova, Vladimir B. Smirnov, Alexander V. Ponomarev

The former is often considered as manifestation of self-similarity of earthquakes occurring at different scales. One of the main parameters measured in the experiments aimed at understanding the laboratory seismicity is the Gutenberg-Richter's "*b*-value" whose variations are interpreted in a relationship with loading conditions and material properties leading to attempts of analogies with natural earthquakes occurrence and their eventual prediction (e.g., Kwiatek et al., 2014).

While built from very large amounts of events, the most of acoustic emission catalogs contain limited numbers of their parameters. In addition to event times, their magnitudes and hypocenter locations (when recorded by a sufficient number of receivers) are most frequently reported. However, the magnitudes are in most of cases determined from records by poorly calibrated sensors and cannot be simply related to physical source parameters. So far, advanced analyses requiring well characterized source spectra, focal mechanisms, etc. are rarely performed on acoustic emission data.

In earthquake seismology, advanced analyses of seismograms and their spectra are used to measure various physical source parameter such as magnitudes, seismic rupture dimensions, seismic energy (e.g., Båth, 1966) and scalar seismic moment (e.g., Aki, 1966). Systematic determination of these different parameters for "regular" tectonic earthquakes resulted in establishing simple scaling relationships between them (e.g., Abercrombie, 1995; Aki, 1967; Kanamori & Anderson, 1975). These "earthquakes scaling laws" remain valid over several orders of magnitudes and lead to a concept of self-similarity of seismic ruptures under constant average stress drop. Together with a simple geometrical argument this gives the Gutenberg Richter distribution with $b = 1$. In this paper, we will refer to a simultaneous observation of the earthquakes scaling laws pointing to constant stress-drop and of *b-value* close to 1 as a "regular earthquake regime".

The average stress drops inferred for tectonic earthquakes approximately lie in the range of 1–10 MPa (equivalent strain drops being between 10^{-5} and 10^{-4}) (e.g., Allmann & Shearer, 2009; Kanamori & Anderson, 1975), which is significantly smaller than the strength of the crustal rocks and the values geologically observed in the field for the faults (Schlische et al., 1996). All this is in good agreement with the conceptual model when tectonic earthquakes are not produced by fresh ruptures but occur on pre-existing and on average "weak" faults.

At the same time, there are various types of seismicity with properties different from the "regular earthquake regime" mentioned above. One example are the volcanic earthquakes that often do not follow the Gutenberg Richter distribution with $b = 1$ (e.g., Galina et al., 2020; Jacobs & McNutt, 2010; Wyss et al., 1998) Another example is provided by the induced seismicity with reported stress drops found to be comparable with tectonic ones (e.g., Huang et al., 2017) as well as being very variable (e.g., Lengliné et al., 2014; Shapiro & Dinske, 2021; Q. Wu et al., 2018). Finally, the scaling laws for recently discovered slow earthquakes are often reported being different from those known for "regular" earthquakes (e.g., Bostock et al., 2015; Farge et al., 2020; Ide & Beroza, 2023; Ide et al., 2007; Peng & Gomberg, 2010). Also, some studies have found deviations from "regular" scaling laws for tectonic earthquakes (Mayeda et al., 2007). Such behavior might be considered as manifestations of different seismogenic mechanisms and mechanical behaviors of involved rocks.

An accurate interpretation of analyses of the laboratory acoustic emission and its comparison with different types of natural seismicity would benefit from more systematically determined physical source parameters similar to approaches used in the earthquake seismology. To achieve this, the spectral analysis of acoustic emission signals is sometimes performed to measure the event seismic moments and corner frequencies (inversely proportional to source time duration and its linear size). However, such an analyses is not routine. The reason is various limitations of laboratory experiment, including resonance of acoustic piezo-transducers, complicated absolute calibration, limited frequency range, limited sample sizes and, accordingly, the configuration of the transducer recording system.

The absolute estimations of corner frequencies and seismic moments was obtained by McLaskey and Lockner (2016) with calibrating sensors on the impact spectrum of a falling steel ball. The laser calibration of sensors was carried out by Yoshimitsu et al. (2014) and Marty et al. (2023) to obtain source characteristics of bigger set of AE-events. In (Yoshimitsu et al., 2014) the cubic relation between seismic moment and source duration has been verified but in the same time the b-value of Gutenberg-Richter has been estimated as two. Results of Marty et al. (2023) have shown the stress-drops tending to increase for larger events. The similar problem has been revealed in Blanke et al. (2020). Harrington and Benson (2011) obtained cubic moment-duration relation for dry

experiment and strong deviation from it in wet samples. Overall, the verification of "earthquake" scaling laws for these small laboratory-scale sources remains an open question.

With the available laboratory experiment performed on relatively small samples, the use of direct waves as it has been done in all works mentioned above is impossible due to the limitations that will be described in detail in the section "Limitations of laboratory AE-signal." Therefore, in this work the use of the signal's coda is proposed as alternative to direct waves, though coda-waves were sometimes implicitly used before in mixture with direct waves: (e.g., McLaskey & Lockner, 2016; B. S. Wu & McLaskey, 2019). In earthquakes seismology, such coda-based approach was successfully applied for estimation of earthquake source spectra (e.g., Baltay et al., 2010; Mayeda & Walter, 1996; Rautian & Khalturin, 1978). Although the acoustic coda in laboratory experiments has a slightly different formation mechanism (e.g., Farin et al., 2016; T. I. Kartseva et al., 2022) it still can be used to estimate the source spectra and their main parameters. To validate the method, we apply it to the data of two experiments: (a) on granite from the Voronezh crystal massif and (b) on Berea sandstone.

2. Earthquake Scaling Laws and Spectral Analysis

The seismic moment M_0 is defined as:

$$M_0 = \mu S D \tag{1}$$

where μ is the shear modulus, S is the rupture surface, and D is the slip amplitude (Aki, 1966). Therefore, M_0 is related to the source size giving rise to a physical magnitude scale (Hanks & Kanamori, 1979):

$$M_W = 2/3 \lg M_0 + const \tag{2}$$

One of the main scaling laws is the relationship between seismic moment and the linear rupture dimension L (or rupture surface) (Kanamori & Anderson, 1975):

$$M_0 \sim L^3 \sim S^{3/2} \tag{3}$$

Combination of Equations 1 and 3 implies the constant average stress drop during earthquakes:

$$\Delta\sigma = C\mu D/L = const \tag{4}$$

where C is a non-dimensional geometrical shape factor and D/L being a strain drop. By combining Equations 2 and 3 we obtain that under constant strain (stress) drop the magnitude is linearly proportional to the logarithm of the rupture surface with a proportionality coefficient equal to 1.

Following (Kanamori & Anderson, 1975), more small ruptures can be accommodated on a total fault area Σ. In other words the product of number of earthquakes N_S with source area S and of this area should be approximately equal to the total fault area: $N_S S \sim \Sigma$, implying that N_s is inversely proportional to the source area. When combined with the linear proportionality between the magnitude and the logarithm of the source area under constant stress drop, this gives the Gutenberg Richter distribution with $b = 1$:

$$\lg N = -bM_w + a, \quad b = 1 \tag{5}$$

For most of earthquakes, the rupture linear dimensions cannot be directly measured. Instead, the source duration in time t_c, that is approximately equal to L/V_r (V_r being the rupture propagation velocity) can be inferred from analyzing seismograms or their spectra. The latter can be corrected for the propagation effects and the radiation pattern to retrieve the frequency dependent source term. The form of this term can be predicted from simple source models (e.g., Boatwright, 1980; Brune, 1970; Haskell, 1964) and is characterized by two asymptotics. At low frequencies, the displacement spectra converges to a plateau whose level is proportional to the seismic moment. At high frequencies, the spectral amplitude is characterized by a power-law decay. The transition between this two asymptortics occurs at the vicinity of so called cut-off or corner frequency f_c that is inversely proportional to the source time duration. As a consequence, the invariance of the seismic rupture stress drop can be expressed via a scaling relationship between the seismic moment and the corner frequency (e.g., Aki, 1967):

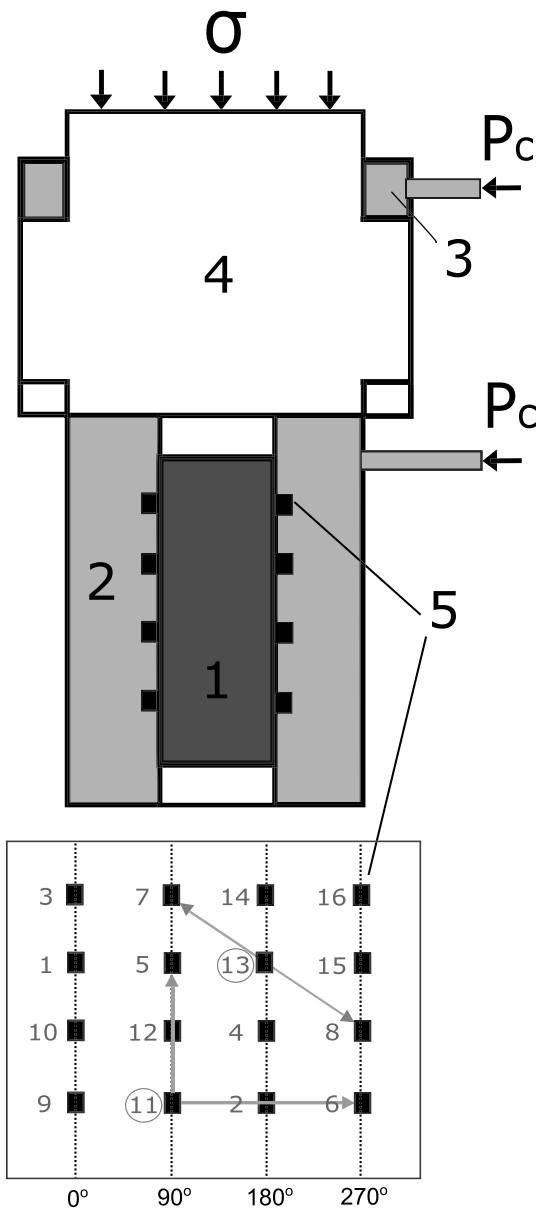

Figure 1. Schematic representation of the experimental set-up. 1—rock sample; 2—confining pressure chamber; 3—compensator providing external pressure equal to *Pc* at the top of the sample; 4—press providing axial load σ; 5—system of 16 piezo-sensors (layout is shown at the bottom). At the bottom: numbers of sensors in gray, examples of ultrasonic sounding traces of two emmiters 11 and 13 sending elastic impulse to corresponding receivers 5 and 6, 7 and 8.

$$M_0 \sim f_c^{-3} \quad (6)$$

Analysis of spectra has been applied to many real seismic data sets and the cubic moment—corner frequency relation has been observed for large and moderate (e.g., Allmann & Shearer, 2009; Ross & Ben-Zion, 2016) to small (with $M_W < 3$) (e.g., Abercrombie, 1995; Prieto et al., 2004) earthquakes, and for the mine and large scale laboratory acoustics (events of magnitudes $M_W < 0$) (e.g., Goodfellow & Young, 2014; Kwiatek et al., 2011; McLaskey et al., 2014; Selvadurai, 2019). The spectral method of determination of source parameters has been also applied to slow earthquakes (e.g., Bostock et al., 2015; Farge et al., 2020; Supino et al., 2020).

3. Data

3.1. Set-Up and Experiments

We use the acoustic data recorded during pseudo-triaxial tests of cylindrical rock samples, carried out on the controlled hydraulic press INOVA-1000 GO "Borok" IPE RAS (A. Patonin et al., 2014; A. V. Patonin et al., 2019). The cylindrical sample of 60 mm height and 30 mm diameter is sealed against penetration of confining oil to the pore space and installed in a cell with 16 ultrasonic sensors. The diameter of sensor body is around 5 mm, the contact surface is curved in accordance to the sample surface and tightly pressed to it. The cell is installed inside the confining pressure chamber and placed between the punches of press (Figure 1).

We consider two experiments that were carried out on Berea sandstone (porosity 17%) and Voronezh granite samples (porosity 0.6%) with similar loading conditions that can be divided into four similar stages (Figure 2). First stages of both experiments are the same: applying four confining pressure P_c steps (+2 MPa, +2 MPa, +4 MPa, +4 MPa) to the intact rock samples. During the stages II the differential stress σ is applied under constant P_c and controlled by the acoustic emission activity to provide quasi-static fault growing. These stages differ in two experiments because of different reaction of samples to the loading. While in Sandstone experiment after reaching around 90% of sample's strength the macro-fault was formed instantly, the Granite sample was able to sustain a cycle of slips along fault, since the axial load was released each time there was a strong increase in acoustic activity. During stages III another four steps 2 MPa each were applied to the damaged rock samples. This stage has strengthen samples (note the increase in P-wave velocities) before final axial loading IV.

Acoustic emission is recorded by a system of side sensors with low-noise pre-amplifying and analog-to-digital converter (ADC) programmed for the pre-triggering mode (sampling rate 2.5 MHz). The acoustic signal is continuously digitized into the ring buffer of ADC. Right after the first signal arrival exceeding the amplitude threshold from any of 16 channels the data block containing 255 μs before the first arrival and 360 μs after is sent to the storage. Therefore for each event with the signal amplitude enough to trigger the system there are 16 waveforms of 615 μs duration with the start time shifted to 255 μs of the standard record frame (Figures 3a and 3b). Noise and signal Fourier amplitude spectra (Figures 3e and 3f) for corresponding records from the first three sensors demonstrate the frequency range limitation: up to around 30 kHz by the noise of the hydraulic press and above around 600 kHz by strong absorption of waves starting from about 600 kHz.

Besides recording of acoustic emission the system is periodically (around each 22 s) switched to the ultrasonic sounding mode. In this mode during the period of 1.5–22 s 8 sensors serve as emitters of artificial elastic impulse

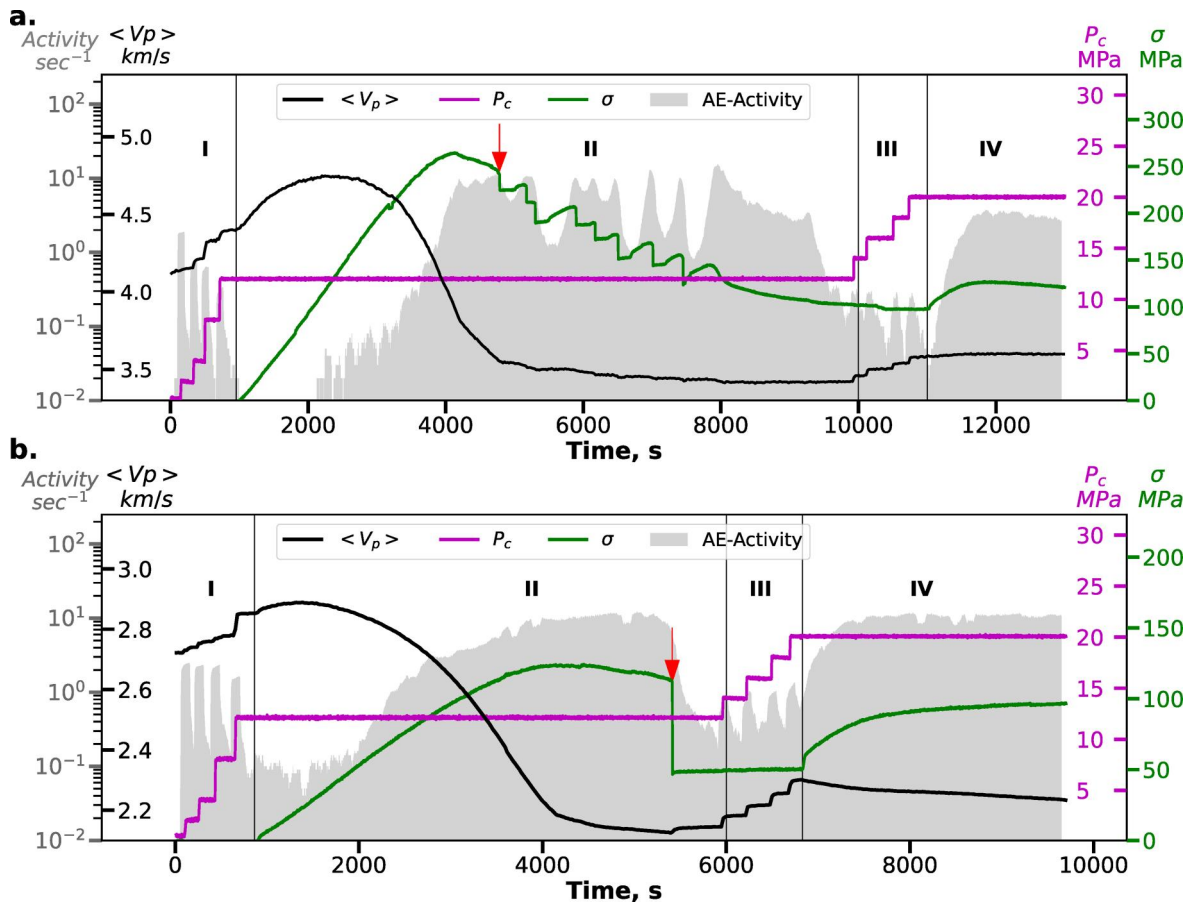

Figure 2. Loading history of Garnite (a) and Sandstone (b) experiments divided by four stages I–IV. *Left axis*: black curves $< V_p >$—P-wave velocities averaged over 16 traces, gray bars showing activity of acoustic emission calculated as 100 events divided by the time period they occur. Red arrows point the onset of macro-faulting (4781s for Granite and 5411s for Sandstone). *Right axis*: magenta curves P_c—confining pressure, green curves σ—differential stress (Figure 1).

while other eight ones receive these signals crossing the sample in different directions (Figure 1). Having a total 16 paths and measured travel times every 22 s allows to calculate time-dependent distribution of elastic wave velocities, that is necessary for the event location procedure. Time evolution of average P-wave velocities is shown with black lines in Figure 2. Location of AE-events is based on automatic determination of arrival times of AE-signals using Akaike Information Criterion (AIC-picker) (Maeda, 1985) and minimizing travel times on all sensors while searching the location on the 1 mm space grid in the sample (for details see A. Patonin et al. (2014)).

During the four stages of granite and sandstone experiments 36,162 and 53,698 acoustic emission waveforms were recorded, respectively.

3.2. Limitations of Laboratory AE-Signals

The experimental setup that we use has several limitations in terms of the quality of the acoustic emission waveforms. The first one and most obvious is clipping of the signals of strongest AE-events due to the limited dynamic range of the ADC (Figure 3b). The second limitation consists in the inability to separate clearly direct waves from the coda (waves reflected from the sample surfaces). Main reason for this is the small size of the sample that is comparable with the used wavelengths. Resulting arrival times of the reflected waves are around 10–15 μs (60 mm/(3.5–4)*km/s*) which is very close to the duration of the direct waves signal (Figures 3a and 3b).

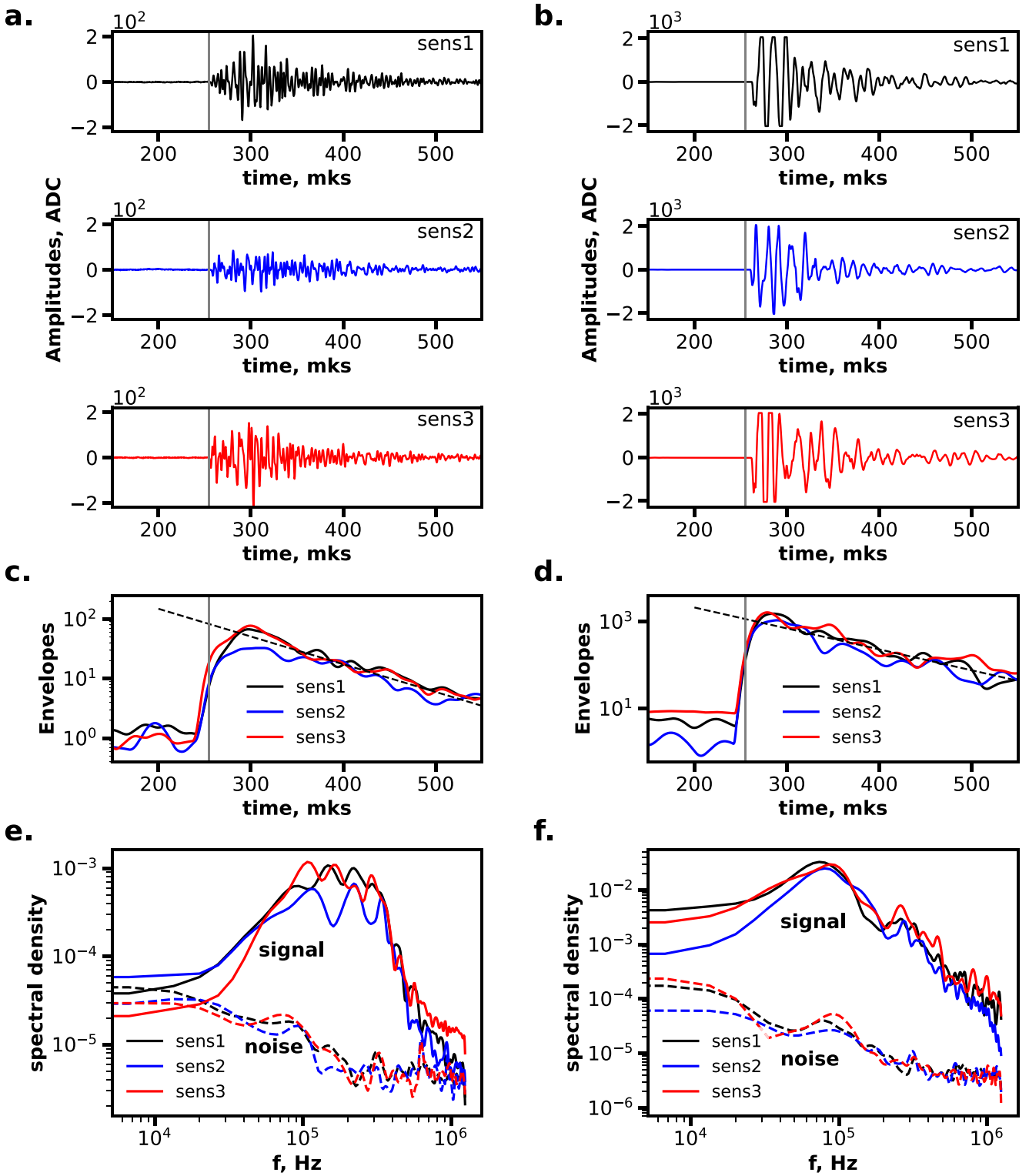

Figure 3. Examples of signals of a relatively weak (a) and a relatively strong (b) acoustic emission events. Recordings from sensors 1, 2, and 3 indicated in the bottom of Figure 1 are shown. Note the clipping of a signal amplitudes on (b). (c and d) Amplitude envelopes of records shown in (a) and (b) in the same color-code obtained by smoothing signal amplitudes with a 100 points long Hanning window (40 μs). The dotted black lines indicate the linear approximation of coda parts (320 − 500 μs) averaged over three sensors. Vertical lines mark the first arrival of event's signal (255 μs). (e and f) Fourier amplitudes (same colors on (a) and (b)). Noise spectra (dotted curves) were calculated from 100 to 250 μs windows. Signal spectra (solid curves) from 250 to 400 μs windows.

4. Estimation of Source Parameters From the Coda of AE-Signals

Signal recorded during event i at sensor j can be represented as (McLaskey & Glaser, 2012; Stein & Wysession, 2009):

$$y_i^j(t) = s_i(t_i,t) * g_{i,j}(t - t_i) * r_j(t - t_i) \tag{7}$$

where $s_i(t_i, t)$ is the source time function of an acoustic emission event i that occurs at time t_i, $g_{i,j}(t - t_i)$ is the Green's function characterizing the wave propagation between the source i and sensor j, and $r_j(t - t_i)$ is the response of the receiver j. In the spectral domain this equation becomes:

$$Y_i^j(f) = S_i(f)\, G_{i,j}(f)\, R_j(f) \tag{8}$$

where f is the frequency and $S_i(f)$ is the source spectra that we would like to retrieve. Thus, a deconvolution of the sensor response and of the propagation term must be applied to the recorded signals (or their spectra). In the earthquake seismology and in majority of laboratory studies, the source parameters are most often retrieved from direct waves. This requires knowing the source position (and ideally focal mechanism) to estimate the Green's function. For the AE events recorded during our laboratory experiments this approach is rather problematic because of the poor quality of the direct wave signals mentioned in the previous section and also because of unknown source locations for many of them.

To mitigate this problem, we use an approach that is based on the coda of the signal (e.g., Mayeda & Walter, 1996; Rautian & Khalturin, 1978; Sens-Schönfelder & Wegler, 2006). In seismology, the coda is formed by the waves scattered on the heterogeneities of the lithosphere (e.g., Aki & Chouet, 1975; Sato et al., 2012). The scattering is considered as a random processes leading to a formulation when the energy of wavefield is described with a radiative transfer theory (e.g., Margerin, 2005; Margerin et al., 1998). Based on this, a practical solution for a coda can be obtained when re-writing Equations 7 and 8 and expressing the Green's functions in terms of energy. For observations this implies that we do not predict the whole signal (including its phase) but rather its envelope. When considering the scattering within the Earth's lithosphere the time dependence of the coda envelope can be approximated with a combination of an exponent and a power-low decays.

In the laboratory experiments, the geometry of coda formation is different comparing to the Earth's lithosphere. Instead of an infinite half-space the waves propagate within a small sample and are very quickly reflected at its boundaries. The coda is mostly formed by these multiple reflected waves. This reverberation is randomized because of the heterogeneities within the sample and on its boundaries. After a few reflections the wavefield can be approximated as diffuse with an energy nearly uniformly distributed over the sample (e.g., Kanev, 2011; Weaver, 1984). This is illustrated with an AE event shown in Figures 3a and 3c when the amplitude of direct waves (arriving at 255–300 μs) can significantly differ from one sensor to another (because of varying source-receiver distances and radiation patterns of both source and receiver) and becomes more homogeneous in the coda (after ∼320 μs). The energy is systematically lost at reflections and also due to the anelastic attenuation within the sample. As a result, its level decays exponentially in time (e.g., Farin et al., 2016) as illustrated with dashed lines in Figures 3c and 3d. The energy decay rate considerably depends on frequency with high frequency waves attenuating faster. This is again illustrated in comparing envelopes in Figures 3c and 3d. For a weaker event (c) whose spectrum contains more high frequencies, the coda amplitudes decay faster than for larger event shown in (d) with more low frequencies. Finally, the coda can be better described with an energy (or amplitude) envelope computed after applying a narrow-band filter. In this case, Equations 7 and 8 can be rewritten as:

$$a_i^j(f,t) = a_0\, S_i(f)\, e^{-\alpha(f)\,(t-t_i)}\, R_j(f) \tag{9}$$

where t is time, $a_i^j(f,t)$ is the coda amplitude envelope computed from a signal recorded at receiver j during event i and bandpassed around frequency (f). a_0 is a factor depending on the experiment geometry, that is, on the shape and the size of the sample that affect the timing of wave reflections. $\alpha(f)$ is the frequency dependent coda decay rate. As described in the following section, we use the system of Equation 9 to retrieve the source spectra $S_i(f)$ (in a relative sense) from records of many events by multiple sensors. For this goal, the equations are linearized by

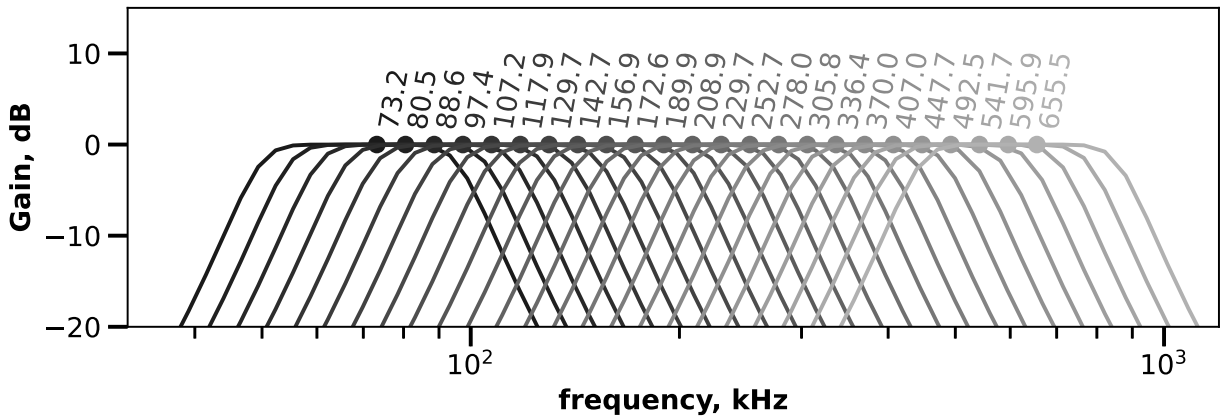

Figure 4. Amplitude responses of set of narrow-band Butterworth filters of 4th order used in this study. Corresponding central frequencies f_0 are noted above. Upper and lower cut-off frequencies of the filters (at −3 dB level) calculated as $f_0 - f_0/3$ and $f_0 + f_0/3$. The sequence of central frequencies is produced as $f_0^i = 1.1 \cdot f_0^{i-1}$.

taking their logarithms. Then, the idea is to compute the bandpassed envelopes from observed signals and to fit parameters of the model Equation 9 in a least-squares sense. As described in the following section, this approach can be used to estimate the source spectral ratios. The last step, is to fit these estimations with a theoretical source model to extract corner frequencies and relative seismic moments.

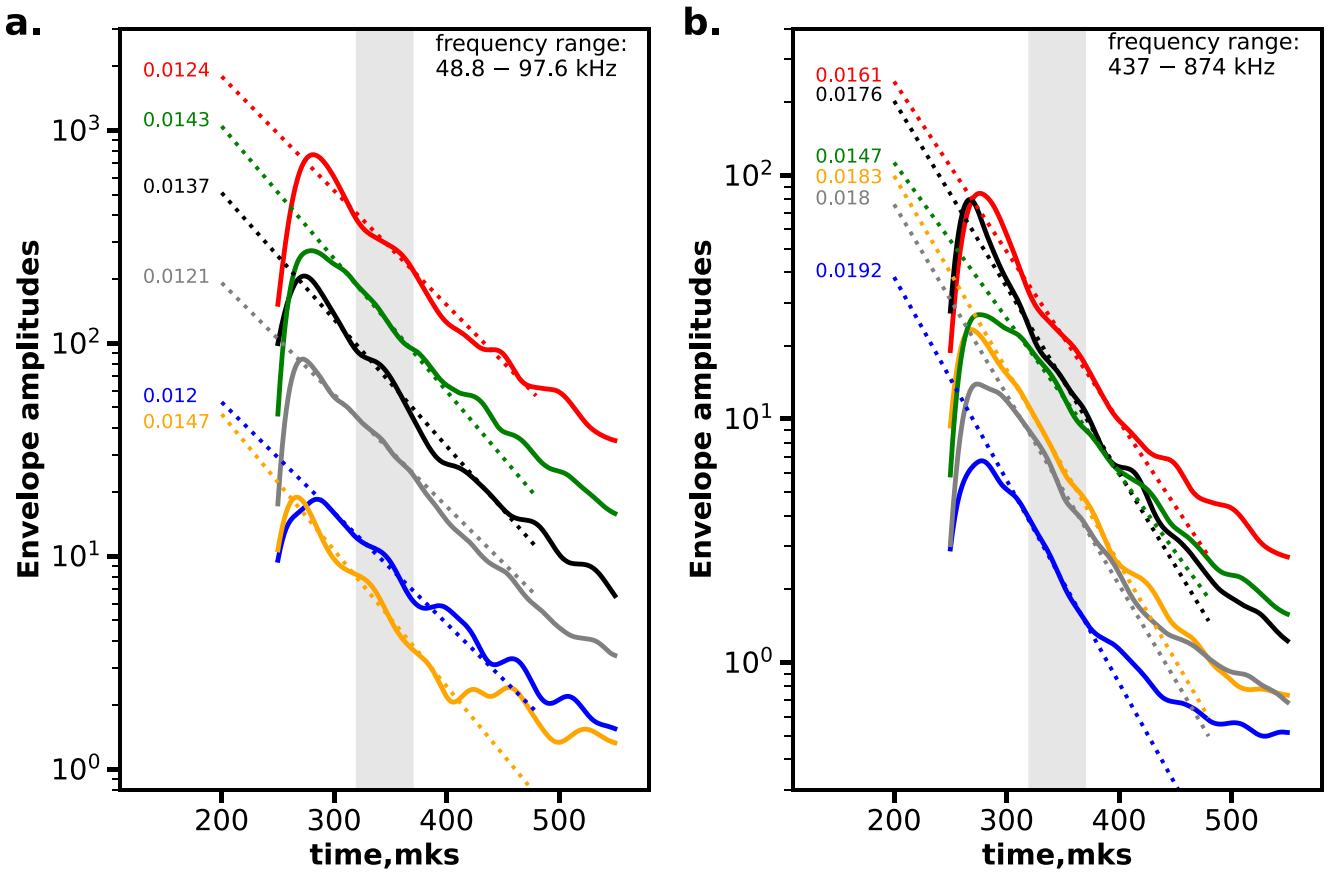

Figure 5. Coda amplitude envelopes of several events (from Stage I of Granite experiment) averaged over 16 sensors and their linear approximations: pre-filtered in 48.8–97.6 kHz (a), 437 − 874 kHz (b). Red curves correspond to the larger event from Figure 3 and blue ones to smaller. Gray area marks the segment of the envelopes chosen for linear approximations. Corresponding $\alpha_i(f)$ (Figure 9) posed near each line.

5. Methods

5.1. Computing Amplitude Envelopes

We start with applying to signals a set of narrow-band Butterworth filters of 4th order whose amplitude responses are shown on Figure 4. Envelopes (amplitudes of Hilbert transforms) of all bandpassed signals are then smoothed with a 100 points long Hanning window (40 μs). Examples of envelopes are shown in Figure 5.

5.2. Selecting the Coda Window

The triggered recording system is set up in a such way that 255 μs before each AE event are kept in memory implying that starting event time in every window is 255 μs. We consider that an average of 5–10 reflections after first arrival are needed to form a diffuse coda. Based on this, we empirically defined the beginning time for our data at 320 μs.

The end of the coda depends on the magnitude of the event and frequency range Figure 5b. In order to save a sufficient amount of information for a stable analysis, while not allowing distortion of the estimates of the coda parameters due to capturing a section with noise, we adopt a simple approach to use a constant window with length of 50 μs for all events and frequency ranges (as indicated with the shaded area in Figure 5).

5.3. Estimating Coda Decay Together With Source and Receiver Factors

The computed coda envelopes at every frequency f $a_i^j(f,t_k)$ (where t_k are time samples within the selected coda window) are fit to model Equation 9 in order to estimate coda decay together with source and receiver factors. After taking logarithm this gives:

$$\lg a_i^j(f,t_k) = B_i(f) - \alpha(f)\lg e\, t_k + C_j(f) \tag{10}$$

where $B_i(f) = \lg S_i(f) + C_0(f)$, $C_j(f) = \lg R_j(f) + \lg a_0 + \alpha(f)\lg e\, t_i - C_0(f)$, and $C_0(f)$ is an arbitrary constant.

If we jointly consider N events recorded by M sensors, Equation 10 gives us at every frequency a system of $N \times M \times K$ equation, with $N + M + 1$ unknowns, where $K = 50$ μs/0.4 μs is the number of time samples. However, it remains degenerated because the unknowns B and C cannot be defined separately until the constant C_0 is not fixed. Therefore, to stabilize the system of equations we add a "normalization" condition:

$$\sum_{j=1}^{M} C_j(f) = 0 \tag{11}$$

After introducing this additional condition, we solve system Equation 10 in a least-squares sense to find the coda decay rate $\alpha(f)$ and the relative source and sensor factors $B_i(f)$ and $C_j(f)$.

5.4. Estimation of Corner Frequencies and Relative Seismic Moments

The estimated source parameters $B_i(f)$ cannot be directly used to estimate the absolute source spectra because of the coefficient $C_0(f)$ that is defined independently at each frequency. However, differences between $B_i(f)$ determined for different events is directly related to the source spectra ratios $SR_{i,j}(f)$ (e.g., Rautian & Khalturin, 1978):

$$SR_{i,j}(f) = 10^{(B_i(f) - B_j(f))} = \frac{S_i(f)}{S_j(f)} \tag{12}$$

We then use a theoretical source model to fit the observed spectral ratios and to estimate main source parameters. The simplest Brune's function (Brune, 1970) appeared not to be a best description of the observed spectral ratios since the degree of spectrum decay at frequencies above f_c is higher than 2. In our analysis, we prefer the Boatwright's model (e.g., Abercrombie, 1995; Boatwright, 1980; Ross & Ben-Zion, 2016) in the form:

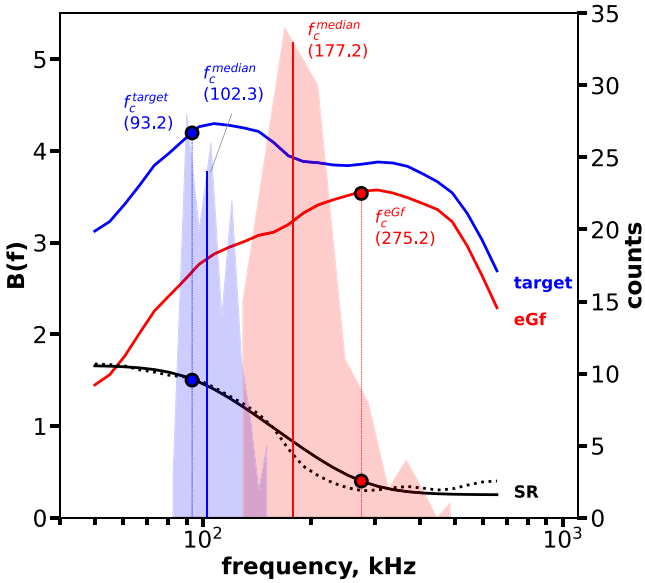

Figure 6. *Left axis*: spectra $B(f)$ and spectral ratio of two events from Figure 3 (large-target in blue line, small-eGf in red line, their spectral ratio SR in doted black line). Boatwright approximation of spectral ratio ($\gamma = 2$, $n = 3$) is in black solid line. *Right axis*: corner frequency histograms for these events obtained from many spectral ratio pairs. Blue and red circles on SR and both $B(f)$ spectra curves mark estimated corner frequencies, corresponding vertical lines mark positions of these particular estimations in the resulting histograms. Solid vertical lines on histograms indicate the medians that are accepted as the best estimations of corner frequencies for both events.

$$S(f) = \frac{C M_0}{\left(1 + \left(\frac{f}{f_c}\right)^{\gamma n}\right)^{1/\gamma}} \tag{13}$$

where M_0 is the seismic moment, f_c is the corner frequency, C is a normalization coefficient, and γ and n are constants describing the spectral fall-off. In our case, the values $\gamma = 2$, $n = 3$ were found to better fit the observations. Deviations from $n = 2$ model have been also observed for earthquakes (Eulenfeld et al., 2022; Eulenfeld & Wegler, 2016; Uchide & Imanishi, 2016). Theoretical expression for the spectral ratio between sources i and j becomes:

$$\frac{S_i(f)}{S_j(f)} = dM_0^{ij}\left(\frac{1 + \left(\frac{f}{f_c^j}\right)^{\gamma n}}{1 + \left(\frac{f}{f_c^i}\right)^{\gamma n}}\right)^{\frac{1}{\gamma}} \tag{14}$$

where $dM_0^{ij} = M_0^i / M_0^j$ is the relative seismic moment.

In a next step, we use non-linear least-squares fitting implemented in a function "CurveFit" of "Optimize" package of "SciPy" library (Virtanen et al., 2020) to find parameters (f_c^i,f_c^j, and dM_0^{ij}) of this theoretical model that better fit the observed spectral ratios Equation 12. An example is shown in Figure 6.

5.5. Routine Analyses of Spectral Ratios

During the experiments lasting around several hours, and, depending on the loading program, signals of tens of thousands of AE events from 16 sensors were recorded. Feeding all this data simultaneously into the system of Equation 10 is not computationally optimal. More importantly, these equations are valid only when the coda decay rates $\alpha(f)$ and the sensor coefficients $R(f)$ remain constant for all considered AE events. This condition, however, cannot be fulfilled during the whole experiment during which the rock samples become strongly damaged and fractured resulting in significant variations of α. Also, strong variations of the confining pressure and loading stresses can modify the coupling between the sensors and the sample resulting in varying effective sensor responses. Therefore, we decided to process the event by relatively small groups ($N = 100$) corresponding to short time intervals during which α and R can be considered as constant.

After selecting a group of $N = 100$ events and estimating $B_i(f)$, they are sorted in descending order using B_i(117 kHz) as a scale since this characteristic is closer to the seismic moment estimated at low-frequencies. Then the spectral ratios are calculated for all possible pairs larger and smaller events that we call "target" and "eGf" (empirical Green's function), respectively. Then these "target-eGf" spectral ratios are fitted with Equation 14 to obtain estimates of relative seismic moments and respective corner frequencies. These estimates are considered stable only for pairs with spectral ratio increasing toward low frequencies and satisfying two following conditions: $\lg\left(f_c^{eGf}\right) - \lg\left(f_c^{target}\right) \geq 0.05$ and $dM_0^{target,eGf} > 1.2$.

Finally, each event of the group is involved in several "target-eGf" pairs resulting in multiple estimations of its seismic moment relative to other event and of its corner frequency. We then analyze this ensemble of estimations statistically to define a most likely values of these parameters.

From all corner frequencies available for a given event, from both the target and eGf roles the median of the f_c distribution calculated as approximation of the true corner frequency (Figure 6). The errors are estimated as 95% confidence interval with lower bound calculated as quantile cutting 2.5% of f_c distribution and the upper bound as quantile cutting 97.5%.

Ensemble of estimations of relative seismic moments gives a system of equations:

$$\lg dM_0^{ij} = \lg M_0^i - \lg M_0^j \tag{15}$$

The number of equations in this system is equal to number of spectral ratios which is larger than the number of unknown $\lg M_0^i$ (number of events, $N = 100$ in our case). Therefore, this systems can be solved in a least-squares sense. However, this system of equation only include differences between logarithms of moments and, therefore, requires an additional normalization condition to be solved. Finally, only relative values of seismic moments for the considered group of AE events are obtained.

Therefore, when processing many groups of events we need to make them overlap to end up with comparable values of seismic moments for the whole ensemble of analyzed event. We use groups with a 50% overlapping. The re-normalization of seismic moments in every new group is made based on the values estimated for 50 overlapping events estimated in the previous group. The first group is normalized by subtracting the minimal resulting $\lg M_0^k$.

We compute a mean difference between logarithms of moments for $N/2$ events present both in group I (earlier in experiment) and group II (later in experiment):

$$\overline{\Delta \lg(M_0)} = \frac{1}{N/2}\sum_{k=1}^{N/2}\left(\lg\left(M_0^k\right)_{II} - \lg\left(M_0^{k+N/2}\right)_I\right) \tag{16}$$

Then, all seismic moments of group II are recalculated according to this correction:

$$\lg\left(M_0^i\right)'_{II} = \lg\left(M_0^i\right)_{II} + \overline{\Delta \lg(M_0)}, \tag{17}$$

Finally, for the $N/2$ overlapping events we recalculate seismic moments as average from two estimations:

$$\lg\left(M_0^k\right)'' = 1/2\left(\lg\left(M_0^k\right)'_{II} + \lg\left(M_0^{k+N/2}\right)_I\right) \tag{18}$$

where k varies from 1 to $N/2$.

For the corner frequencies the values of the overlapping events are also modified. The median and corresponding quantiles are recalculated with accounting for the new f_c statistics coming from the group II.

5.6. Quality Control and Event Selection

At different steps of the analysis described above, several criteria of events selection are applied resulting in reduction of the final amount of AE-events with estimated source parameters:

1. Preliminary rejection of weak signals (average coda envelope amplitude at 320 *mks* less then 300*ADC*)
2. During the short period 5404 − 5415s of Sandstone experiment 100 events were removed from the analyses since there were many overlapping waveforms because of fast development of the macro-fault
3. On the stage of spectral ratio parameters f_C^i, f_c^j and dM_0^{ij} estimation there imposed several criteria for selection of good pairs of events: (a) $dM_0^{ij} > \frac{S_i\left(2f_c^j\right)}{S_j\left(2f_c^j\right)}$ (see Equation 14), (b) $\lg\left(f_c^j\right) - \lg\left(f_c^i\right) \geq 0.05$, (c) $dM_0^{ij} > 1.2$, where index i is responsible for "target" event and j for "eGf." The condition (a) roughly checks the spectrum shape and for the best performance of spectral ratio method the difference between corner frequencies and their magnitudes of events are imposed via (b) and (c).
4. For statistical significance of the final estimation we consider events for which the amount of successful spectral ratios (that passed condition Equation 3) is larger than 20

While applying first two criteria rejected 19% in Granite experiment and 31% in Sandstone experiment, the third and fourth ones reduced for other 25% and 36%, respectively. Finally, we kept 56% of AE events for Granite and 33% for Sandstone.

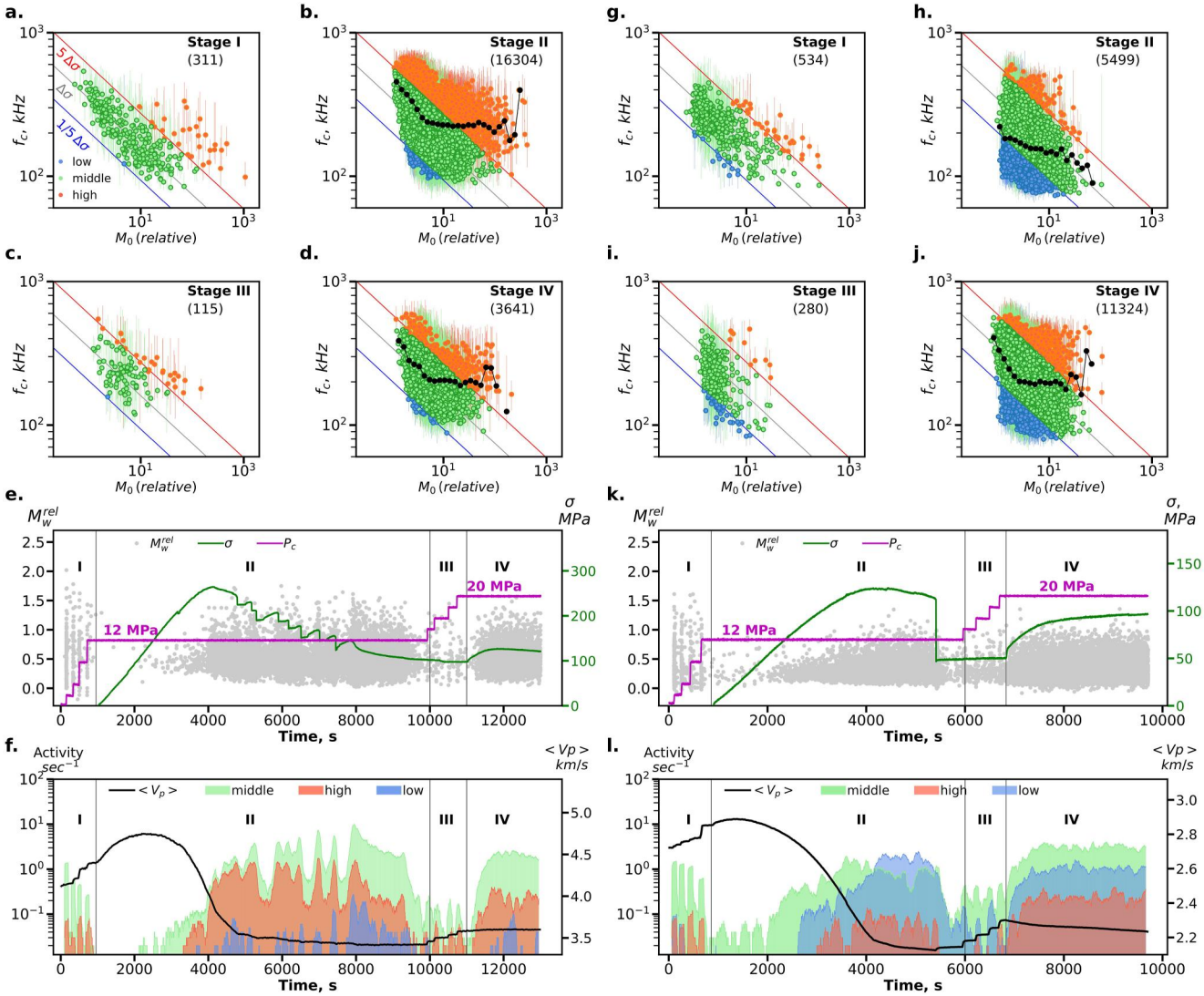

Figure 7. Results for Granite (left a–f), Sandstone (right g–l). Diagrams f_c versus M_0 for I–IV stages of Granite (a–d) and Sandstone (g–j): gray line - stress-drop reference $\left(f_c \sim M_0^{-1/3}\right)$, blue and red—5-fold decrease and increase of reference stress-drop respectively, numbers in brackets assign the amount of events in current stage. Color of circles with error bars assigns position of point relative to stress-drop lines: ≤1/5Δσ—blue (low), between 1/5Δσ & 5Δσ—green (middle), ≥5Δσ—red (high). Black curves on (b), (d), (h), (j) show average corner frequencies per moment bin (bins are 0.1 in logarithm). (e and k) *Left axis*: relative M_w (Figure 2)—gray points. *Right axis*: differential stress σ—green curve. Confining pressure P_c—pink curve (more detailed on Figure 2). (f and l) *Left axis*: activity (event/sec) of events with different stress-drops. Color of each bar-plot corresponds to the color of group on (a–d) and (g–j) panels. *Right axis*: black curves show averaged over 16 traces P-wave velocity changes.

6. Results

After analyses of all records in both experiments and all applied criteria of selection there left: 20,372 (56%) events in Granite experiment, 17,638 (33%) events in Sandstone experiment. The general difference in amount of events left in analyses mainly caused by the preliminary massive rejection of weak signals. In the sandstone sample the relation of small events to large is higher than in the granite.

Figures 7a and 7g show the results for AE events recorded during the Stage I. During initial ~900 s of both experiments four steps of increasing isotropic confining pressure were applied to the samples. No macro-scale rock damage was observed in this period. It can be seen that during this stage most of events approximately align along a $f_c \sim M_0^{-1/3}$ scaling. However, there is a group of events in Figure 7a, mainly having relative seismic moments larger than 100, that deviate significantly from the general trend. These large events have corner

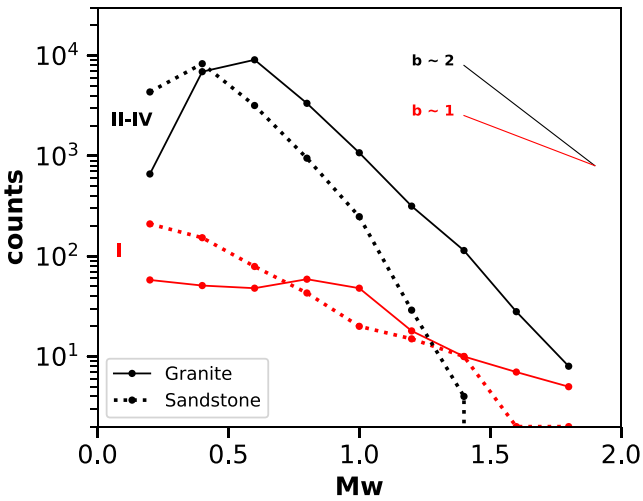

Figure 8. Gutenberg-Richter distributions of relative M_w for Granite (solid), Sandstone (dotted) on Stages I—in red, Stages II–IV in black. Lines in right-upper corner with different slopes (*b–values*) for comparison. Note that M_w are relative either between experiments.

frequencies exceeding those predicted by the $f_c \sim M_0^{-1/3}$ trend. As discussed in Section 7, this deviation is likely caused the limited frequency bandwidth of acoustic records.

We also compute relative moment magnitudes (Equation 2 with $const = 0$) for these events and plot the magnitude frequency distribution in Figure 8 with red lines. During the initial stages of both experiments (Granite and Sandstone) this distribution follow the power-law Gutenberg-Richter distribution with $b - value$ close to one. Overall, the behavior of AE events recorded during these first stages has strong similarities with the tectonic earthquakes and likely corresponds to rupturing pre-existing micro-fractures characterized by approximately constant stress drop. The level of this stress drop, however, cannot be established because of the lack of absolute values of seismic moments.

Several examples of eGf-corrected stacked spectra of target events from Stage I of both experiments are presented in Figure 9. Each of these spectra S_i is obtained by stacking spectral ratios of given target i with the set of its best eGfs j normalized by the corresponding eGf's seismic moment $SR_{i,j}(f)M_0^j$ (Equations 12, 14 and 15). While four spectra of events lying close to the constant stress-drop line Figure 9a demonstrate scaling similar to one described by Aki (1967), the other two events with higher corner frequencies (blue and orange) considerably deviate from this scaling.

For the interpretation of the AE emission recorded during all stages of the experiments, we set-up the position of the line $f_c = 70kHz \cdot \left(\frac{120}{M_0}\right)^{1/3}$ on log-log scale crossing the majority of events of Stage I (Figures 7a and 7g, gray line), as a reference relative stress drop.

This level corresponds to initial conditions within the undamaged samples. Events significantly deviating from this line and lying above or below it are then considered to have larger or smaller stress drops, respectively.

Stages II of both experiments started with applying increasing axial load under constant confining pressure (Figures 7e and 7k). This load gradually increases until the condition of formation of a macro-fracture of the samples are reached. This was followed by a decrease in the axial load, gradual in the case of granite and step-like in the case of sandstone. During stages III, the confining pressure is again increasing. Stages IV consist of additional increase of axial load under fixed confining pressure.

Two projections of AE-events locations (method described in Section 3.1) on fault cross-sections during the Stages I and in the periods of 1000s after initiation of macro-faults shown in Figure 10 demonstrate difference between rock types. For the granite Figure 10a event locations on the Stage I tend to orient along one direction while in the sandstone Figure 10b locations from the first stage distributed around the whole volume of the sample and only after the failure events locations aligned in the plane of the slip.

After active fracturing during Stages II, the Stages III is designed to consolidate the sample by applying steps of confining pressure similar to that of Stages I but with the presence of non-changing axial load. The level of "stress-drop" during this stage is similar to Stages I with most of events concentrating around reference $\Delta\sigma$ (Figures 7c and 7i). However, these stages are depleted in large-scale events.

In contrast to the Stages I and III the estimations from the Stages II and IV demonstrate large diversity of stress-drops. If the gray line assigns the reference level of constant stress-drops $\Delta\sigma$ based on Stage I, the red and blue lines represent 5-fold increase and decrease in stress-drop, respectively. Statistical distribution compiled during all four stages (Figure 11) demonstrate that in granite the overall stress-drop is higher than the initial reference level and inverse situation is observed in the sandstone sample.

The dynamics of stress-drops with highly variable experimental conditions is shown in Figures 7f and 7l with color of each bar-plot linked to the corresponding group of events in Figures 7a–7d and 7g–7j. Above mentioned balance between high and low stress drop events in both experiments is clearly observed with some details in

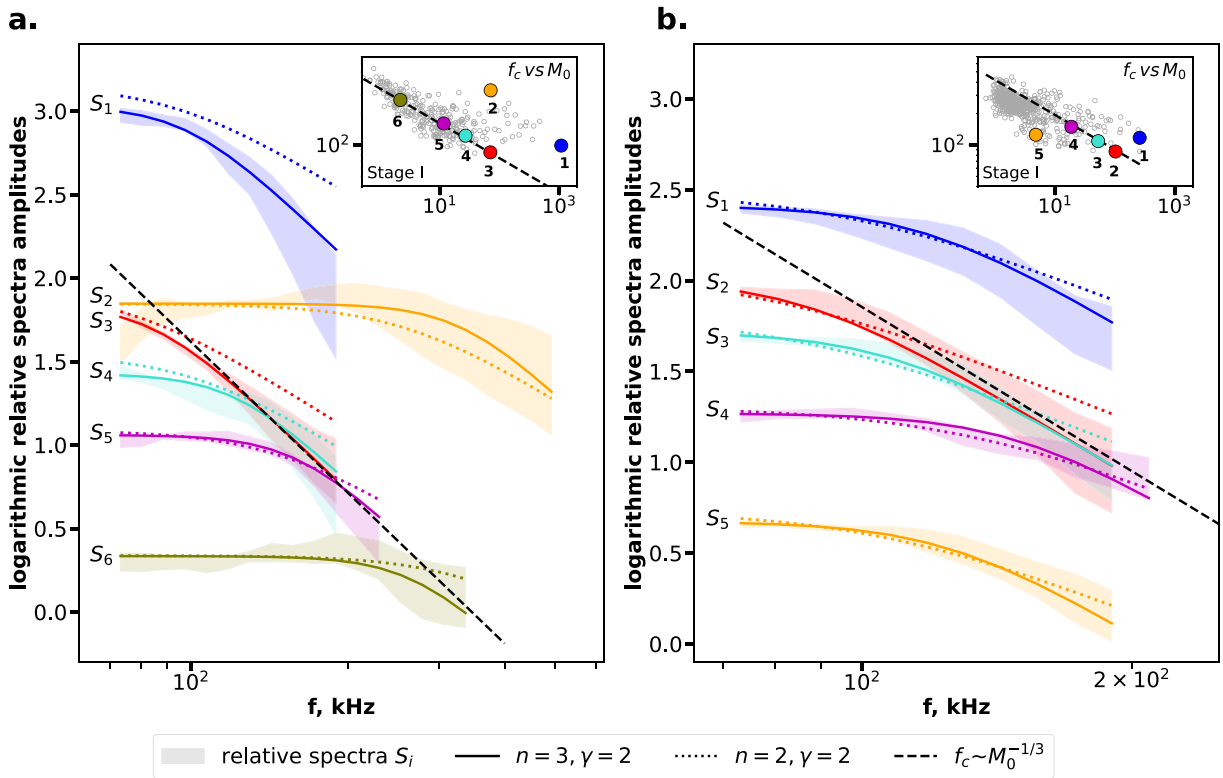

Figure 9. Examples of eGf-corrected normalized stacked spectra from Stage I of Granite (a) and Sandstone (b). The target events chosen for spectra demonstration are marked with colored points on the inserts showing Stage I diagrams identical to Figures 7a and 7g. The number of each target event corresponds to the number of spectra S_1–S_6 for granite and S_1– S_5 for sandstone. The spectra bands S_i represent the variation of eGf corrected normalized spectra set for a given *ith* target (around 5–10 for each target). Because of specific procedure of estimation of final f_c and M_0 that is based on the set of parameters without strict separation of events on "targets" and "eGfs" and selection of successful spectral ratios (Section 5.6) the amount of appropriate pairs of chosen targets with their eGfs is quite small, especially, if demonstrating group of targets of equal stress-drop, that is, following the same cubic line $f_c \sim M_0^{-1/3}$ (dashed lines). Two spectra decay rate $n = 3$ and $n = 2$ of Boatwright model with $\gamma = 2$ also presented. While M_0^j of $n = 3$ model was used here for normalizing spectral ratios, it is seen that seismic moment estimations of both models are quite similar unlike the corner frequencies.

temporal variability that can reflect the internal changes during fracturing process (Figures 7f and 7l). In the Granite experiment, initiation of damage and formation of the micro-fracture is associated with appearance of many "high stress drop" events that remain nearly dominating (with numbers very close to "normal stress drop" events) till the axial load is reduced to the pre-fracture level (at ~8,000 s). In the sandstone, the initiation of damage at ~3,000 s is associated with the "low stress drop" events that persist till the release of the axial load at ~6,000 s and then re-appear in stage IV when the axial load is increased again. We note, that this kind of dynamics that could not be retrieved from "standard" analyses based on occurrence times and magnitudes.

The Gutenberg-Richter distributions obtained during Stages II–IV in granite and sandstone are shown in Figure 8 with black solid and dashed lines, respectively, have much higher *b–values*. The magnitudes of completeness are higher than during Stage I, which is explained by the selection criteria imposed on the f_c differences in spectral ratios (Section 5.5 "Routine analyses of spectral ratios") and less amount of events satisfying these criteria particularly on Stages II. Nevertheless, the *b-values* observed during these later stages are significantly higher than 1.

7. Discussion and Conclusions

In this paper we described a new approach to estimate the relative source spectra of AE events from codas of signals recorded during laboratory experiments. The respective spectral ratios can be used to estimate main source parameters: corner frequencies f_c and relative seismic moment M_0. The decay of the coda amplitude envelopes is described with a simple diffuse approximation (e.g., Farin et al., 2016). In small samples, the diffuse wavefield is

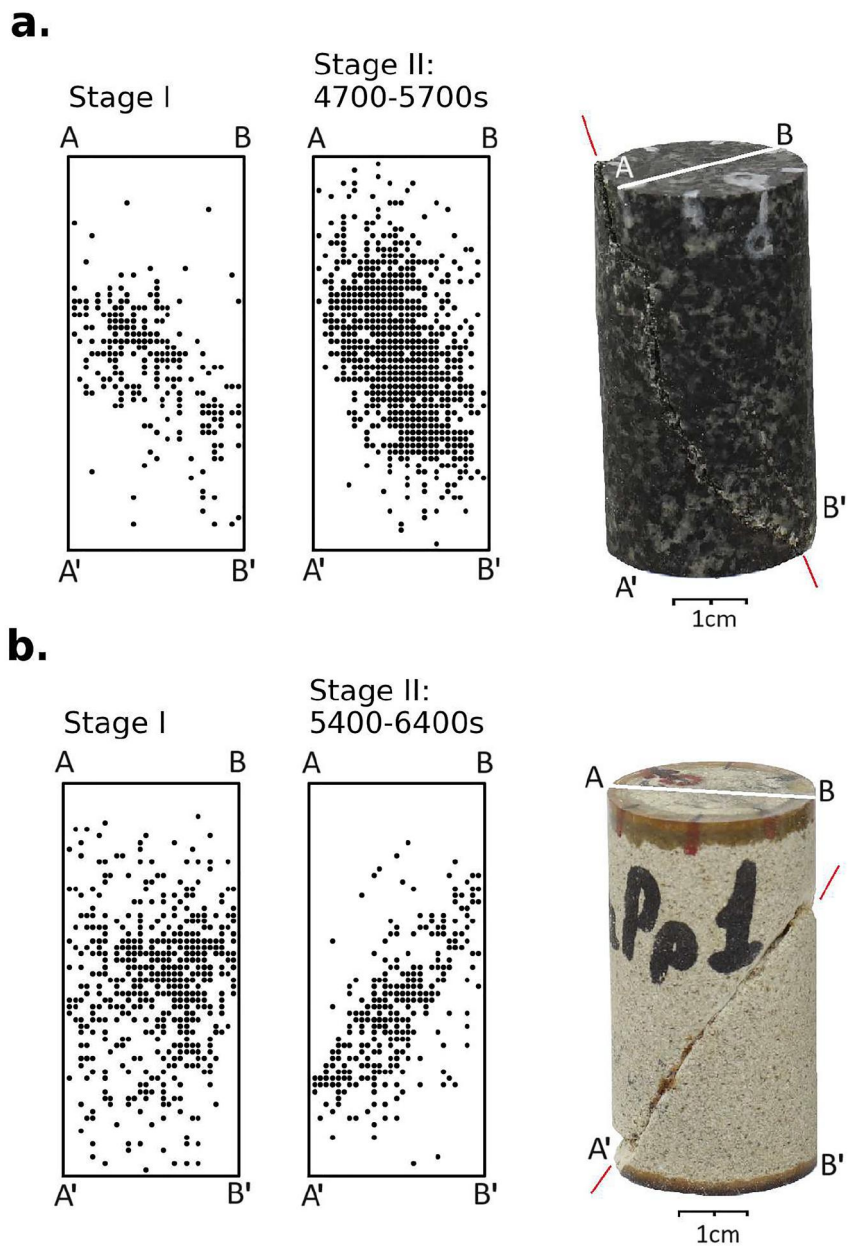

Figure 10. Location of AE-events (Section 3.1) with the photos of samples after experiments a—Granite and b—Sandstone. Locations were projected on sample cross sections AA'B'B normal to the fault plane. The periods from which locations were taken are marked above the corresponding panels. Orientation of macro-faults are marked by red arrows.

mainly formed by multiple reverberations leading to a nearly homogeneous distribution of energy across the media. This implies equal amplitude level and decay rate at all sensors, independent of their position and the source location and mechanism. Overall, the proposed coda based source spectra estimation have an advantage of being relatively simple, that is, it does not require information about the source locations and mechanisms, separation of direct P and S waves, and well calibrated acoustic recording system. Therefore, it can be potentially applied to many experiments run on relatively small rock samples.

We validated the developed method by applying to AE signals recorded during two experiments described in Section 3 "Data." With the selected data quality criteria (Section 5.6 "Quality Control and Event Selection") we could determine the relative seismic moments and corner frequencies for 30–60% of all recorded AE events. As a

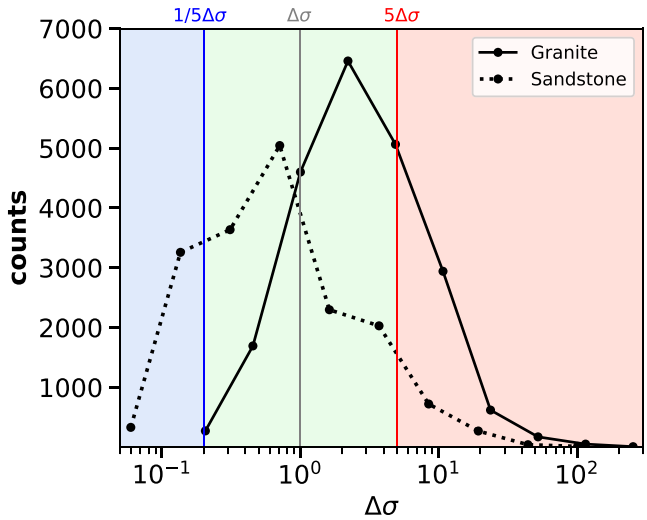

Figure 11. Distribution of apparent stress-drops in both experiments. Vertical lines correspond to that of the lines on Figures 7a–7d and 7g–7j with colored area assigning the ranges of low (blue), middle (green) and high (red) stress-drops.

main result, the AE catalogs were enriched with two additional physical parameters such as corner frequency f_c and relative seismic moment M_0 whose evolution as function of loading conditions could be studied.

We were particularly interested in verifying if the recorded AE events followed a behavior similar to regular earthquakes that are known to exhibit nearly constant stress-drop independent of their size and to obey a Gutenberg-Richter law with *b-values* close to 1. For this goal, we investigated two observable relationships: (a) the scaling between the seismic moment and the corner frequency, and (b) the Gutenberg-Richter distribution computed from moment magnitudes M_W. In the "regular earthquake regime", the scaling is expected to be cubic (Equation 6) and the *b-value* being close to one.

We have found that two above mentioned attributes of the "regular earthquake regime" have been approximately verified during initial stages of both experiments when the rock samples were loaded with increasing isotropic confining pressure. The origin of the AE during this stage is most likely related to the inhomogeneity of the rock samples that results in a heterogeneous internal stress distributions even under an isotropic loading. The AE events can be triggered at the stress concentrators such as preexisting microfaults, pores or grain boundaries having high contrast in physical properties (Anders et al., 2014). The observed similarity with natural earthquakes can be interpreted that these Stage I AE events mostly occur on preexisting micro faults with a nearly constant stress drop. Existence of such preexisting micro faults is partially confirmed by the distribution of AE hypocenters from the experiment in granite (Figure 10a) that start to be aligned even during Stage I.

The behavior of the AE events changes drastically once the samples become significantly damaged and many new micro fractures start to appear under the axial load (Stages II and IV). The dots on the log-log $f_c - M_0$ plane do not align along a line (Figures 7b, 7d and 7h, 7g) but form a "cloud" with appearance of many events whose spectra are either enriched or depleted in high frequencies comparing to the "reference" level observed during Stage I. The *b-value* of the Gutenberg-Richter distribution becomes much larger than 1 (Figure 8 black curves). One possible hypotheses for explaining this is that the *b-value* can be related to the level of stress (e.g., Main et al., 1989; V. B. Smirnov et al., 2019; V. Smirnov & Ponomarev, 2020; Dong et al., 2022).

Overall, the behavior observed during Stages II and IV is very different from the "regular earthquake regime." One important implication of this result is that a direct comparison of laboratory and natural earthquakes is not always appropriate and that in some laboratory regimes, for example, associated with active sample damage, the mechanisms of rock deformation faulting might be very different from natural conditions in the Earth's lithosphere.

Additionally, we observe different behaviors in the experiments performed on different rocks. From the granite experiment we retrieve more events enriched in high frequencies during Stages II and IV (red area in Figure 7f), the activity shifts toward events depleted in high frequencies (red area in Figure 7l) in the sandstone sample. One possibility is to interpret the observed distributions in the $f_c - M_0$ plane in terms of varying stress-drop. Events enriched and depleted in high frequencies (red and blue colors in Figures 7a–7d and 7g–7j) would be associated with the increased and reduced levels of stress-drop, respectively. The increased stress drop events might be associated with creation of new micro faults. The low stress drop level might be associated with re-activation of recently opened fractures or other types of "weak" contacts in the rock. The latter are more likely to be present in the more porous sandstone which could explain the larger relative number of events depleted in high frequencies recorded during this experiment.

Similar to many studies estimating source parameters from amplitude spectra, our results are subject to large uncertainties caused by two main problems: a limited frequency range and a simplistic source model (e.g., Abercrombie, 2021). Therefore, the concept of "stress-drop" should be applied to our results with a certain caution. First, the available frequency range is rather limited because of the sensor bandwidth and, in particular, because of the low-frequency noise from the hydraulic press. The latter could cause the lack of corner frequencies

below ~100 kHz seen in Figure 7. Second, the stress-drop inferred through the seismic moment and corner frequency scaling is based on the ideal earthquake source model that considers the faults with constant rupture propagation speed. The faulting mechanisms within the actively damaged rock samples can be far from this idealization. Source processes of small earthquakes might be heterogeneous which would produce complex spectra (e.g., Abercrombie, 2021) making estimations of corner frequencies with the spectral ratios highly uncertain (Ruhl et al., 2017; Shearer et al., 2019) and biasing the inferred scaling, especially when applied to limited bandwidth data.

Additional important limitation of the results obtained in this study is that absolute values of source parameters could not be estimated. This first concerns the seismic moments. Without knowing their relative values, the $M_0 - f_c$ scaling can be estimated only within the range of measured corner frequencies. However, it cannot be compared with more global trends (e.g., Goodfellow & Young, 2014; Yoshimitsu et al., 2014). To advance in this direction we would need to estimate absolute values of seismic moments for at least a few AE events. This could be eventually achieved with an improved calibration of the recording acoustic system.

Another difficulty is to estimate the spatial extension of the AE event sources. Following the "standard" earthquake model they can be related to corner frequencies as: $L \approx V_r/f_c$. For real earthquakes the rupture speed V_r is known to be close to the shear wave speed, that is, of the order of a few kilometers per second. Applying this to our data would give source dimensions between millimeters and centimeters. In particular, estimations of the source dimensions corresponding to smallest observed corner frequencies (70–100 kHz) would be close to the sample size (3–5 cm). The millimetric to centimetric source sizes do not match the dimensions of micro-fractures measured in samples that are usually associated the grain boundaries and therefore should not exceed the average grain size (Anders et al., 2014). The grains do not exceed 0.3–0.5 mm and 1–2 mm in the Berea sandstone and the granite of Voronezh massif, respectively. This discrepancy could be another indication of the difference between the natural tectonic earthquakes and the fracturing and damaging of the small laboratory rock samples.

Overall, the use of coda waves in the solving the problem of laboratory AE-source characterization seems to be promising. It can become a useful tool to enrich the knowledge about the fracture process.

Data Availability Statement

The numerical data containing raw AE-waveform records, appearance of AE-events in time, loading curves and results (absolute corner frequencies, relative seismic moments and relative stress-drops) used and obtained in this study are available at Zenodo via (T. Kartseva, 2023) with open access.

Acknowledgments
This study was supported by the European Research Council under the European Union Horizon 2020 research and innovation program (Grant 787399-SEISMAZE) and by the Russian Ministry of Education and Science (Grant 14. W03.31.0033 "Geophysical research, monitoring and forecasting of catastrophic geodynamic processes in the Russian Far East"). Experiments carried out in the RESC of IPE RAS "Petrophysics, Geomechanics and Paleomagnetism", Geophysical Observatory "Borok", IPE RAS, according state tasks of the Schmidt Institute of Physics of the Earth, Russian Academy of Sciences, and the Physics Department of Moscow State University.

References

Abercrombie, R. E. (1995). Earthquake source scaling relationships from- 1 to 5 ml using seismograms recorded at 2.5-km depth. *Journal of Geophysical Research*, *100*(B12), 24015–24036. https://doi.org/10.1029/95jb02397

Abercrombie, R. E. (2021). Resolution and uncertainties in estimates of earthquake stress drop and energy release. *Philosophical Transactions of the Royal Society A*, *379*(2196), 20200131. https://doi.org/10.1098/rsta.2020.0131

Aki, K. (1966). Generation and propagation of g waves from the Niigata earthquake of June 16, 1964: Part 2. Estimation of earthquake moment, released energy, and stress-strain drop from the g wave spectrum. *Bulletin of the Earthquake Research Institute*, *44*(1), 73–88.

Aki, K. (1967). Scaling law of seismic spectrum. *Journal of Geophysical Research*, *72*(4), 1217–1231. https://doi.org/10.1029/jz072i004p01217

Aki, K., & Chouet, B. (1975). Origin of coda waves: Source, attenuation, and scattering effects. *Journal of Geophysical Research*, *80*(23), 3322–3342. https://doi.org/10.1029/jb080i023p03322

Allmann, B. P., & Shearer, P. M. (2009). Global variations of stress drop for moderate to large earthquakes. *Journal of Geophysical Research*, *114*(B1). https://doi.org/10.1029/2008jb005821

Anders, M. H., Laubach, S. E., & Scholz, C. H. (2014). Microfractures: A review. *Journal of Structural Geology*, *69*, 377–394. https://doi.org/10.1016/j.jsg.2014.05.011

Baltay, A., Prieto, G., & Beroza, G. C. (2010). Radiated seismic energy from coda measurements and no scaling in apparent stress with seismic moment. *Journal of Geophysical Research*, *115*(B8). https://doi.org/10.1029/2009jb006736

Båth, M. (1966). Earthquake energy and magnitude. *Physics and Chemistry of the Earth*, *7*, 115–165. https://doi.org/10.1016/0079-1946(66)90003-6

Blanke, A., Kwiatek, G., Goebel, T. H. W., Bohnhoff, M., & Dresen, G. (2020). Stress drop magnitude dependence of acoustic emissions during laboratory stick-slip. *Geophysical Journal International*, *224*(2), 1371–1380. https://doi.org/10.1093/gji/ggaa524

Boatwright, J. (1980). A spectral theory for circular seismic sources; simple estimates of source dimension, dynamic stress drop, and radiated seismic energy. *Bulletin of the Seismological Society of America*, *70*(1), 1–27. https://doi.org/10.1785/BSSA0700010001

Bolton, D. C., Marone, C., Saffer, D., & Trugman, D. T. (2023). Foreshock properties illuminate nucleation processes of slow and fast laboratory earthquakes. *Nature Communications*, *14*(1), 3859. https://doi.org/10.1038/s41467-023-39399-0

Bostock, M. G., Thomas, A. M., Savard, G., Chuang, L., & Rubin, A. M. (2015). Magnitudes and moment-duration scaling of low-frequency earthquakes beneath southern Vancouver Island. *Journal of Geophysical Research: Solid Earth*, *120*(9), 6329–6350. https://doi.org/10.1002/2015JB012195

Brune, J. N. (1970). Tectonic stress and the spectra of seismic shear waves from earthquakes. *Journal of Geophysical Research*, *75*(26), 4997–5009.

Dong, L., Zhang, L., Liu, H., Du, K., & Liu, X. (2022). Acoustic emission b value characteristics of granite under true triaxial stress. *Mathematics*, *10*(3), 451. https://doi.org/10.3390/math10030451

Eulenfeld, T., Dahm, T., Heimann, S., & Wegler, U. (2022). Fast and robust earthquake source spectra and moment magnitudes from envelope inversion. *Bulletin of the Seismological Society of America*, *112*(2), 878–893. https://doi.org/10.1785/0120210200

Eulenfeld, T., & Wegler, U. (2016). Measurement of intrinsic and scattering attenuation of shear waves in two sedimentary basins and comparison to crystalline sites in Germany. *Geophysical Journal International*, *205*(2), 744–757. https://doi.org/10.1093/gji/ggw035

Farge, G., Shapiro, N. M., & Frank, W. B. (2020). Moment-duration scaling of low-frequency earthquakes in Guerrero, Mexico. *Journal of Geophysical Research: Solid Earth*, *125*(8), e2019JB019099. https://doi.org/10.1029/2019jb019099

Farin, M., Mangeney, A., de Rosny, J., Toussaint, R., Sainte-Marie, J., & Shapiro, N. M. (2016). Experimental validation of theoretical methods to estimate the energy radiated by elastic waves during an impact. *Journal of Sound and Vibration*, *362*, 176–202. https://doi.org/10.1016/j.jsv.2015.10.003

Galina, N. A., Shapiro, N. M., Droznin, D. V., Droznina, S. Y., Senyukov, S. L., & Chebrov, D. V. (2020). Recurrence of deep long-period earthquakes beneath the klyuchevskoi volcano group, Kamchatka. *Izvestiya - Physics of the Solid Earth*, *56*(6), 749–761. https://doi.org/10.1134/S1069351320060026

Goodfellow, S. D., & Young, R. P. (2014). A laboratory acoustic emission experiment under in situ conditions. *Geophysical Research Letters*, *41*(10), 3422–3430. https://doi.org/10.1002/2014GL059965

Gutenberg, B., & Richter, C. F. (1944). Frequency of earthquakes in California. *Bulletin of the Seismological Society of America*, *34*(4), 185–188. https://doi.org/10.1785/BSSA0340040185

Hanks, T. C., & Kanamori, H. (1979). A moment magnitude scale. *Journal of Geophysical Research*, *84*(B5), 2348–2350. https://doi.org/10.1029/JB084iB05p02348

Harrington, R. M., & Benson, P. M. (2011). Analysis of laboratory simulations of volcanic hybrid earthquakes using empirical green's functions. *Journal of Geophysical Research*, *116*(B11). https://doi.org/10.1029/2011jb008373

Haskell, N. A. (1964). Total energy and energy spectral density of elastic wave radiation from propagating faults. *Bulletin of the Seismological Society of America*, *54*(6A), 1811–1841. https://doi.org/10.1785/BSSA05406A1811

Huang, Y., Ellsworth, W. L., & Beroza, G. C. (2017). Stress drops of induced and tectonic earthquakes in the central United States are indistinguishable. *Science Advances*, *3*(8), e1700772. https://doi.org/10.1126/sciadv.1700772

Ide, S., & Beroza, G. C. (2023). Slow earthquake scaling reconsidered as a boundary between distinct modes of rupture propagation. *Proceedings of the National Academy of Sciences of the United States of America*, *120*(32), e2222102120. https://doi.org/10.1073/pnas.2222102120

Ide, S., Beroza, G. C., Shelly, D. R., & Uchide, T. (2007). A scaling law for slow earthquakes. *Nature*, *447*(7140), 76–79. https://doi.org/10.1038/nature05780

Jacobs, K. M., & McNutt, S. R. (2010). *Using seismic b-values to interpret seismicity rates and physical processes during the preeruptive earthquake swarm at Augustine volcano 2005–2006: Chapter 3 in the 2006 eruption of Augustine Volcano, Alaska* (Tech. Rep.). US Geological Survey.

Kanamori, H., & Anderson, D. L. (1975). Theoretical basis of some empirical relations in seismology. *Bulletin of the Seismological Society of America*, *65*(5), 1073–1095. https://doi.org/10.1785/BSSA0650051073

Kanev, N. (2011). Sound decay in a rectangular room with specular and diffuse reflecting surfaces. In *Proceedings of Forum Acusticum* (pp. 1935–1940).

Kartseva, T. (2023). Acoustic data and loading regime of two rock physics experiments carried out on inova-1000 test-complex, borok, Russia [Dataset]. *Zenodo*. https://doi.org/10.5281/zenodo.10036388

Kartseva, T. I., Shapiro, N. M., Patonin, A. V., Smirnov, V. B., & Ponomarev, A. V. (2022). Energy classification of acoustic events using the coda of a signal. *Seismic Instruments*, *58*(1), 18–25. https://doi.org/10.3103/s0747923922010054

Kwiatek, G., Goebel, T., & Dresen, G. (2014). Seismic moment tensor and b value variations over successive seismic cycles in laboratory stick-slip experiments. *Geophysical Research Letters*, *41*(16), 5838–5846. https://doi.org/10.1002/2014gl060159

Kwiatek, G., Plenkers, K., & and, G. D. (2011). Source parameters of picoseismicity recorded at mponeng deep gold mine, South Africa: Implications for scaling relations. *Bulletin of the Seismological Society of America*, *101*(6), 2592–2608. https://doi.org/10.1785/0120110094

Lengliné, O., Lamourette, L., Vivin, L., Cuenot, N., & Schmittbuhl, J. (2014). Fluid-induced earthquakes with variable stress drop. *Journal of Geophysical Research: Solid Earth*, *119*(12), 8900–8913. https://doi.org/10.1002/2014JB011282

Lockner, D., Byerlee, J., Kuksenko, V., Ponomarev, A., & Sidorin, A. (1991). Quasi-static fault growth and shear fracture energy in granite. *Nature*, *350*(6313), 39–42. https://doi.org/10.1038/350039a0

Maeda, N. (1985). A method for reading and checking phase times in autoprocessing system of seismic wave data. *Zisin*, *38*(3), 365–379. https://doi.org/10.4294/zisin1948.38.3_365

Main, I. G., Meredith, P. G., & Jones, C. (1989). A reinterpretation of the precursory seismic b-value anomaly from fracture mechanics. *Geophysical Journal International*, *96*(1), 131–138. https://doi.org/10.1111/j.1365-246x.1989.tb05255.x

Margerin, L. (2005). Introduction to radiative transfer of seismic waves. In *Seismic earth: Array analysis of broadband seismograms* (pp. 229–252). American Geophysical Union (AGU). https://doi.org/10.1029/157GM14

Margerin, L., Campillo, M., & Tiggelen, B. (1998). Radiative transfer and diffusion of waves in a layered medium: New insight into coda Q. *Geophysical Journal International*, *134*(2), 596–612. https://doi.org/10.1111/j.1365-246X.1998.tb07142.x

Marty, S., Schubnel, A., Bhat, H., Aubry, J., Fukuyama, E., Latour, S., et al. (2023). Nucleation of laboratory earthquakes: Quantitative analysis and scalings. *Journal of Geophysical Research: Solid Earth*, *128*(3), e2022JB026294. https://doi.org/10.1029/2022jb026294

Mayeda, K., Malagnini, L., & Walter, W. R. (2007). A new spectral ratio method using narrow band coda envelopes: Evidence for non-self-similarity in the hector mine sequence. *Geophysical Research Letters*, *34*(11), L11303. https://doi.org/10.1029/2007GL030041

Mayeda, K., & Walter, W. R. (1996). Moment, energy, stress drop, and source spectra of Western United States earthquakes from regional coda envelopes. *Journal of Geophysical Research*, *101*(B5), 11195–11208. https://doi.org/10.1029/96JB00112

McLaskey, G. C., & Glaser, S. D. (2012). Acoustic emission sensor calibration for absolute source measurements. *Journal of Nondestructive Evaluation*, *31*(2), 157–168. https://doi.org/10.1007/s10921-012-0131-2

McLaskey, G. C., & Kilgore, B. D. (2013). Foreshocks during the nucleation of stick-slip instability. *Journal of Geophysical Research: Solid Earth*, *118*(6), 2982–2997. https://doi.org/10.1002/jgrb.50232

McLaskey, G. C., Kilgore, B. D., Lockner, D. A., & Beeler, N. M. (2014). Laboratory generated m-6 earthquakes. *Pure and Applied Geophysics*, *171*(10), 2601–2615. https://doi.org/10.1007/s00024-013-0772-9

McLaskey, G. C., & Lockner, D. A. (2016). Calibrated acoustic emission system records m -3.5 to m -8 events generated on a saw-cut granite sample. *Rock Mechanics and Rock Engineering*, *49*(11), 4527–4536. https://doi.org/10.1007/s00603-016-1082-1

Omori, F. (1894). On the aftershocks of earthquakes. *Journal of the College of Science, Imperial University of Tokyo*, *7*, 111–120.

Patonin, A., Ponomarev, A., & Smirnov, V. (2014). A laboratory instrumental complex for studying the physics of the destruction of rocks. *Seismic Instruments*, *50*(1), 9–19. https://doi.org/10.3103/s0747923914010046

Patonin, A. V., Shikhova, N. M., Ponomarev, A. V., & Smirnov, V. B. (2019). A modular system for continuous recording of acoustic emission for laboratory studies of rock destruction processes. *Seismic Instruments*, *55*(3), 313–326. https://doi.org/10.3103/s0747923919030101

Peng, Z., & Gomberg, J. (2010). An integrated perspective of the continuum between earthquakes and slow-slip phenomena. *Nature Geoscience*, *3*(9), 599–607. https://doi.org/10.1038/ngeo940

Prieto, G. A., Shearer, P. M., Vernon, F. L., & Kilb, D. (2004). Earthquake source scaling and self-similarity estimation from stacking spectra. *Journal of Geophysical Research*, *109*(B8). https://doi.org/10.1029/2004jb003084

Rautian, T., & Khalturin, V. (1978). The use of the coda for determination of the earthquake source spectrum. *Bulletin of the Seismological Society of America*, *68*(4), 923–948. https://doi.org/10.1785/bssa0680040923

Ross, Z. E., & Ben-Zion, Y. (2016). Toward reliable automated estimates of earthquake source properties from body wave spectra. *Journal of Geophysical Research: Solid Earth*, *121*(6), 4390–4407. https://doi.org/10.1002/2016jb013003

Ruhl, C. J., Abercrombie, R. E., & Smith, K. D. (2017). Spatiotemporal variation of stress drop during the 2008 mogul, Nevada, earthquake swarm. *Journal of Geophysical Research: Solid Earth*, *122*(10), 8163–8180. https://doi.org/10.1002/2017JB014601

Sato, H., Fehler, M., & Maeda, T. (2012). *Seismic wave propagation and scattering in the heterogeneous Earth* (2nd ed.). Springer. https://doi.org/10.1007/978-3-642-23029-5

Schlische, R. W., Young, S. S., Ackermann, R. V., & Gupta, A. (1996). Geometry and scaling relations of a population of very small rift-related normal faults. *Geology*, *24*(8), 683–686. https://doi.org/10.1130/0091-7613(1996)024⟨0683:GASROA⟩2.3.CO;2

Scholz, C. H. (1968). Experimental study of the fracturing process in brittle rock. *Journal of Geophysical Research*, *73*(4), 1447–1454. https://doi.org/10.1029/JB073i004p01447

Selvadurai, P. A. (2019). Laboratory insight into seismic estimates of energy partitioning during dynamic rupture: An observable scaling breakdown. *Journal of Geophysical Research: Solid Earth*, *124*(11), 11350–11379. https://doi.org/10.1029/2018jb017194

Sens-Schönfelder, C., & Wegler, U. (2006). Radiative transfer theory for estimation of the seismic moment. *Geophysical Journal International*, *167*(3), 1363–1372. https://doi.org/10.1111/j.1365-246X.2006.03139.x

Shapiro, S. A., & Dinske, C. (2021). Stress drop, seismogenic index and fault cohesion of fluid-induced earthquakes. *Rock Mechanics and Rock Engineering*, *54*(10), 5483–5492. https://doi.org/10.1007/s00603-021-02420-3

Shearer, P. M., Abercrombie, R. E., Trugman, D. T., & Wang, W. (2019). Comparing EGF methods for estimating corner frequency and stress drop from p wave spectra. *Journal of Geophysical Research: Solid Earth*, *124*(4), 3966–3986. https://doi.org/10.1029/2018JB016957

Smirnov, V., & Ponomarev, A. (2020). Physics of transient seismicity regimes. *Russain Academy of Sciences*.

Smirnov, V. B., Ponomarev, A. V., Stanchits, S. A., Potanina, M. G., Patonin, A. V., Dresen, G., et al. (2019). Laboratory modeling of aftershock sequences: Stress dependences of the Omori and Gutenberg–Richter parameters. *Izvestiya - Physics of the Solid Earth*, *55*(1), 124–137. https://doi.org/10.1134/S1069351319010105

Stein, S., & Wysession, M. (2009). *An introduction to seismology, earthquakes, and Earth structure*. John Wiley & Sons.

Supino, M., Poiata, N., Festa, G., Vilotte, J.-P., Satriano, C., & Obara, K. (2020). Self-similarity of low-frequency earthquakes. *Scientific Reports*, *10*(1), 1–9. https://doi.org/10.1038/s41598-020-63584-6

Uchide, T., & Imanishi, K. (2016). Small earthquakes deviate from the omega-square model as revealed by multiple spectral ratio analysis. *Bulletin of the Seismological Society of America*, *106*(3), 1357–1363. https://doi.org/10.1785/0120150322

Virtanen, P., Gommers, R., Oliphant, T. E., Haberland, M., Reddy, T., Cournapeau, D., et al. (2020). SciPy 1.0: Fundamental algorithms for scientific computing in Python. *Nature Methods*, *17*(3), 261–272. https://doi.org/10.1038/s41592-019-0686-2

Weaver, R. L. (1984). Diffuse waves in finite plates. *Journal of Sound and Vibration*, *94*(3), 319–335.

Wu, B. S., & McLaskey, G. C. (2019). Contained laboratory earthquakes ranging from slow to fast. *Journal of Geophysical Research: Solid Earth*, *124*(10), 10270–10291. https://doi.org/10.1029/2019jb017865

Wu, Q., Chapman, M., & Chen, X. (2018). Stress-drop variations of induced earthquakes in Oklahoma. *Bulletin of the Seismological Society of America*, *108*(3A), 1107–1123. https://doi.org/10.1785/0120170335

Wyss, M., McNutt, S. R., & Wyss, M. (1998). Temporal and three-dimensional spatial analyses of the frequency–magnitude distribution near long valley caldera, California. *Geophysical Journal International*, *134*(2), 409–421. https://doi.org/10.1046/j.1365-246x.1998.00561.x

Yoshimitsu, N., Kawakata, H., & Takahashi, N. (2014). Magnitude -7 level earthquakes: A new lower limit of self-similarity in seismic scaling relationships. *Geophysical Research Letters*, *41*(13), 4495–4502. https://doi.org/10.1002/2014gl060306